HHS Public Access

Author manuscript

ACS Appl Mater Interfaces. Author manuscript; available in PMC 2018 January 11.

Published in final edited form as:

ACS Appl Mater Interfaces. 2017 January 11; 9(1): 101–111. doi:10.1021/acsami.6b11304.

Silica-Coated Metal Chelating-Melanin Nanoparticles as a Dual-Modal Contrast Enhancement Imaging and Therapeutic Agent

Soojeong Cho[†], **Wooram Park**[†], and **Dong-Hyun Kim**[*,†,‡]

[†]Department of Radiology, Feinberg School of Medicine, Northwestern University, Chicago, Illinois 60611, United States

[‡]Robert H. Lurie Comprehensive Cancer Center, Chicago, Illinois 60611, United States

Abstract

Bioinspired melanin nanoparticle (Mel NP) synthesized with dopamine has been of great interest in various biomedical applications. However, the utilization of fascinating characters of Mel NP such as innate MR contrast effects, high affinity to metal ions, strong light absorption requires special design with strategic synthetic method for its own purpose. Here, we have introduced paramagnetic Gd^{3+} metal ions and silica nanocoating on Mel NP for the dual-modal MRI/fluorescent contrast-enhanced imaging and therapeutics. The Gd^{3+} chelating kinetics of Mel NP by quinone and hydroquinone residues were optimized in various conditions of Gd^{3+} amounts and pH in solution for improving MRI contrast enhancing properties of the Mel NP. Then, bioinert silica was coated on the surfaces of Gd-chelated Mel NP (Gd-Mel@SiO_2 NP) with a modified sol–gel process. The silica nanocoating allowed increased outer sphere water diffusion time, resulting a significantly brighter MR T_1 contrast effect of Gd-Mel@SiO_2 NP, comparing with a bare Gd-Mel NP or clinical grade T_1 contrast agent. Further, when the Gd-Mel@SiO_2 NP was labeled with fluorescent molecules, a significantly enhanced fluorescent intensity was achieved by the silica nanocoating that preventing the innate fluorescent deactivation property of melanin. Finally, in vitro/in vivo dual-modal contrast enhanced MRI/fluorescent imaging and feasibility of image-

[*]**Corresponding Author**: dhkim@northwestern.edu.

Supporting Information

The Supporting Information is available free of charge on the ACS Publications website at DOI: 10.1021/acsami.6b11304. Experimental method, size distribution of Mel NPs, data for Gd chelation kinetics including time-dependent change of pH in various Gd^{3+} feeding concentrations, graph for relative number of monomers in Mel NP to chelate one mole of Gd, in saturated state and relation between initial chelation rate and $[Gd]/[H^+]$, SEM image after sol-gel reaction without CTAB on Mel NPs, and zeta potential of Mel, Gd-Mel, Gd-Mel@SiO_2, and Gd-Mel@SiO_2-APTES NPs, TEM images before and after dissolving melanin with H_2O_2, optimization of labeling amount of TRITC on Gd-Mel@SiO_2, T_2 relaxivities of Gd-Mel NPs and Gd-Mel@SiO_2 NPs, fluorescent images and spectra of FITC-labeled Gd-Mel@SiO_2 NPs and TRITC-labeled Gd-Mel@SiO_2 NPs, respectively, data of photothermal transduction property of Gd-Mel and Gd-Mel@SiO_2 NPs including concentration-dependent absorbance, cooling curve of Gd-Mel@SiO_2 NPs, and time-dependent increase in temperature in the solution of Gd-Mel NPs, and Gd-leaching experiment during laser exposure (PDF)

ORCID

Wooram Park: 0000-0002-4614-0530

Dong-Hyun Kim: 0000-0001-6815-3319

Author Contributions

The manuscript was written through contributions of all authors. All authors have given approval to the final version of the manuscript.

Notes

The authors declare no competing financial interest.

guided cancer therapeutic applications using Gd-Mel@SiO_2 NPs were successfully evaluated in a clinically relevant human prostate cancer xenograft mouse model.

Graphical abstract

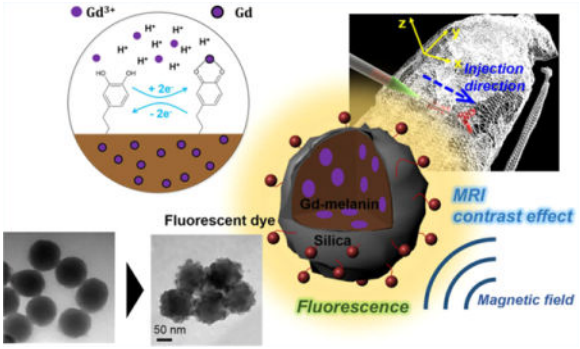

Keywords

melanin; silica coating; metal-chelation; multimodal image-guidance; MRI; fluorescence imaging

INTRODUCTION

Melanin is a light absorptive pigment and a strong radical scavenger, which plays an important role as a body protector from harmful light and toxic substances.[1,2] Its properties of strong light absorption, high affinity to metal ions, biodegradability in the high oxidative stress, photoprotection, and free radical quenching are fascinating in a new class of materials for applications developed from functions.[3–5] Recently, dopamine-derived melanin nanoparticle (Mel NP) has emerged for biomedical applications with its highly biological relevance to natural melanin.[6] Specifically, having considered optical properties of Mel NP, highly efficient photothermal transduction can be achieved with the way our body increases itstemperature in the melanin contained in the skin under strong sunlight.[7] Thus, the Mel NP has been studied for use as efficient photothermal mediators in cancer therapeutics.[8,9] In addition, the high binding capacity of melanin (binding capacity for metal ions 6×10^{20} sites per gram of melanin)[10] to the neighboring contents provides attractive features for metal ion chelation; gadolinium (Gd), copper (Cu), and iron (Fe) components show contrast enhancement effect in magnetic resonance imaging (MRI).[10–12] Metal chelated Mel NP has been reported as potential MRI T_1 and T_2 contrast agents for diagnostics and interventional guidance scanning anatomical planes with comparable spatial and temporal resolution.[10,13,14] However, metal ion chelating kinetics and optimization in Mel NP have yet to be studied for the advanced medical imaging applications. Further, as developing minimally invasive image-guided therapies, combinational imaging approaches using MRI, fluorescent, PET/CT and so on are in demand for more precise diagnostic and intraoperative imaging techniques. However, the strong surface reactivity of Mel NP causes challenges to introduce optical/fluorescent labeling onto Mel NP for a combinational MRI/fluorescent imaging, which is a desirable strong modality for unambiguous identification of specific tumor tissues during interventional local therapies such as photothermal/cryo/irreversible

electroporation (IRE)/radiofrequency ablations,[15–20] and surgical resections.[21] The reactivity of Mel NP in the process of comproportionation equilibrium between o-quinone and o-hydroquinone deactivates the photoexcited electrons of labeled fluorescent molecules.[22–24] Other issues of concern for the bioapplications of Mel NP is the lack of bioavailability due to insoluble forms and toxicity.[25] The active Mel NP causes in vitro and in vivo toxicity by scavenging radicals and ions from biological environments.[2,7] Therefore, the applicable dose of Mel NPs hardly reaches the working concentration range for effective medical imaging and therapeutic applications.[26–28] Currently, functional modification of Mel NPs compromising with innate properties of melanin is strongly required to resolve pending issues in biomedical applications. Mel NPs coated with organic ligands such as poly(vinyl alcohol),[29] polyethylene glycol (PEG),[6] and hyaluronic acid (HA)[30] have been developed to improve bioavailability of Mel NPs. However, aforementioned surface coatings are not permanent and strongly affected by solution pH or temperature as they tend to detach from surfaces depending on solution environment or their dispersion stability.[31,32] To overcome this physicochemical limitations, silica has been utilized in various systems such as metals, semiconductors, magnetic or ceramic nanoparticles for the stability.[33] In addition, the easy regulation of the coating process, chemical inertness, controlled porosity, processability, and optical transparency are other reasons of the use of silica coating.[34] Thus, inorganic silica coating on Mel NPs is strongly considered for enhancing biocompatibility, surface functionality, and aqueous dispersity for biomedical applications.[35,36]

Herein, we developed silica-coated Gd-chelated melanin nanoparticle (Gd-Mel NP) for dual-modal contrast enhanced MRI/fluorescent imaging and cancer therapeutics (Figure 1). Gd chelating kinetics and MR T_1 contrast effects of Mel NP were analyzed for an application of MRI T_1 contrast agents. Then, Gd chelated Mel NPs were coated with various amounts of silica in a controlled manner. Improved solution stability, biocompatibility, and MR/fluorescent contrast enhancement imaging properties of Gd-Mel NP after the silica nanocoating were investigated. Finally, as prepared silica coated Gd-Mel NP (Gd-Mel@SiO_2 NP) was evaluated for in vivo dual-modal MRI/fluorescent imaging contrast enhancement agents for image-guided cancer therapy.

EXPERIMENTAL METHODS

Materials and Reagents

Dopamine hydrochloride, gadolinium-(III) chloride ($GdCl_3$), tetraethyl orthosilicate (TEOS), (3- Aminopropyl) triethoxysilane (APTES), and tetramethylrhodamine isothiocyanate mixed isomers (TRITC) were purchased from Sigma-Aldrich (St. Louis, MO, USA). Sodium hydroxide solution (NaOH, 10 N), cetyltrimethylammonium bromide (CTAB), and ammonium hydroxide solution (NH_4OH, 28–30%) were obtained from VWR International (Radnor, PA, USA). Magnevist (Gadopentetate dimeglumine: Gd-DTPA) was purchased from Bayer (Leverkusen, Germany). Standard cell culture media, Gibco RPMI 1640, was purchased from Thermo Fisher Scientific (Waltham, MA, USA) and CCK-8 solution was obtained from Dojindo Molecular Technologies, Inc. (Kumamoto, Japan).

Preparation of Gd-Mel NPs

Mel NPs were prepared according to the previous literature.[37] First, 100 mL aqueous solution of 9.23 mM dopamine hydrochloride was prepared in a round flask. Once the reaction batch became 50 °C in an oil bath, 528 μL of 1 M NaOH solution was added to the dopamine solution with continuous stirring. Then, the solution immediately turned to brown color and this reaction was proceeded for 3 h. Finally, the synthesized Mel NPs were cooled to room temperature and washed for three times by repeating precipitation using centrifugation at 12 000 rpm and redispersion in fresh distilled water. We prepared samples to observe the chelating property of Mel NPs depending on chelating agent concentrations and pH. The solutions of $GdCl_3$ were prepared their concentrations from 175 to 1054 μM (pH 7). The initial pH conditions were varied from 2 to 9.5 with $GdCl_3$ solution of 879 μM. In the 5 mL suspensions of 400 μg/mL Mel NPs, we added 1 mL solutions of $GdCl_3$ with respective concentrations and incubated the mixed suspensions at 37 °C for 8 h. Then, final suspensions of Gd-Mel NPs were collected and washed thoroughly by repeating purification using centrifugation and redispersion in distilled water. To prepare Gd-Mel NPs for subsequent characterization and applications, we added 5 mL of 1000 μM $GdCl_3$ solution into a 25 mL aqueous suspension (pH 9.5) of Mel NPs with a concentration of 400 μg/mL. Then, the solution was incubated for 8 h at 37 °C and washed by repeating precipitation using centrifugation and redispersion in distilled water. To quantify chelated Gd amounts in Mel NPs, samples of Gd-Mel NPs prepared in aforementioned conditions were dissolved in 3% solutions of nitric acid for Gd elemental analysis using inductively coupled plasma mass spectrometry (ICP-MS, iCAP Q, Thermo Fisher Scientific, Waltham, MA, USA).

Formation of Silica Nanocoating on Gd-Mel@SiO_2 NPs

One milliliter of 0.1 M CTAB solution was added into 10 mL of 3 mg/mL Gd-Mel NP suspension and the mixture was left for 2 h. This aqueous suspension of Gd-Mel NPs was redispersed in ethanol by precipitation with centrifugation and redispersion in ethanol. While continuously stirring, we mixed 30 mL of ethanolic suspension of 0.14 mg/mL Gd-Mel NP with 0.5 mL of NH_4OH solution (28–30%) and adjusted the amount of distilled water from 0 to 2 mL in a round flask to control the amount of silica nanocoating. Then, 400 μL of TEOS was injected with a syringe pump (New Era Pump Systems, Farmingdale, NY, USA) in a flow rate of 100 μL/h. Finally, Gd-Mel@SiO_2 NPs were purified by 3 times repeating washing steps by precipitation with centrifugation and redispersion in ethanol.

Preparation of TRITC-labeled Gd-Mel@SiO_2 NPs

Eleven milliliters of an ethanolic suspension of 6.5 μg/mL Gd-Mel@SiO_2 NPs was mixed with 25 μL of APTES for amine functionalization, initiated by addition of 0.5 mL of NH_4OH in a 20 mL PPE vial. The reaction proceeded for 12 h at room temperature with continuous stirring. Then, amine-functionalized Gd-Mel@SiO_2 NPs were washed by precipitation using centrifugation and redispersion in ethanol. The final concentration of Gd-Mel@SiO_2 NPs was 7.5 μg/mL before fluorescent labeling. The 9 mL suspension of Gd-Mel@SiO_2 NPs was mixed with 1.12 mM TRITC ethanolic solution and purified with repeated centrifugation and redispersion in distilled water.

Characterization of TRITC-labeled Gd-Mel@SiO_2 NPs

TRITC-labeled Gd-Mel@SiO_2 NPs were observed with transmission electron microscopy (TEM, Tecnai Spirit G2, 120 kV, FEI Company, Hillsboro, OR, USA) and scanning and transmission electron microscopy (STEM, HD-2300 Dual EDS Cryo STEM, Hitachi, Tokyo, Japan) for the analysis of morphologies and elemental mapping of Gd and Si. Zeta-potential of nanoparticles was measured with Zetasizer Nano ZSP (Malvern Instruments Ltd., Worcestershire, UK). Gd contents in TRITC-labeled Gd-Mel@SiO_2 NPs were measured with ICP-MS. Paramagnetic property of TRITC-labeled Gd-Mel@ SiO_2 NPs was examined with an MPMS XL-7 superconducting quantum interference device (SQUID) magnetometer (Quantum Design Inc., San Diego, CA, USA) at 300 K. The photothermal property was measured with a fiber-coupled near-infrared (NIR) (808 nm) diode-laser (BWF5, B&W Tek Inc., Newark, DE, USA) by illuminating 1 mL aqueous suspension of TRITC-labeled Gd-Mel@ SiO_2 NPs, contained in a 2 mL glass vial. The various concentration of TRITC-labeled Gd-Mel@SiO_2 NP suspensions were monitored their temperature changes during laser exposure with 188 mW/cm^2: 0, 0.15, 0.3, 0.6, and 1.2 mg/mL. In addition, temperature increase was measured in 0.6 mg/mL suspension of TRITC-labeled Gd-Mel@SiO_2 NPs depending on laser powers with 188, 294, and 464 mW/cm^2. An infrared (IR) thermal camera (ICI7320P, Beaumont, TX, USA) was also used to measure the temperature of suspensions. The photothermal transduction efficiency, which is the conversion efficiency of absorbed light radiation into thermal energy, was determined as described in a previous report and the Supporting Information.[38]

Fluorescence Characterization of TRITC-labeled Gd-Mel@ SiO_2 NPs

To measure surface coverage of TRITC on Gd-Mel@SiO_2 NPs depending on the amount of silica nanocoating, we maintained the number of NPs in each batch by performing a sol–gel reaction starting from the same concentration of Gd-Mel NP: the ratio between distilled water and TEOS was 0, 1.8, 3.0, and 5.5, respectively. In 1 mL ethanolic suspensions of both bare Gd-Mel NPs and APTES-treated Gd-Mel@SiO_2 NPs synthesized in aforementioned conditions, we added 200 μL solutions of TRITC in ethanol with various concentrations: 0.364, 0.73, 1.46, 2.91, 5.83, 11.7, 23.3, and 46 μM. Then, each sample was washed to collect unreacted or free TRITC molecules. We measured absorbance at 569 nm of collected TRITC solutions with UV–visible spectrometer (Citation 3 Automated Microscope Plate Reader, BioTek Inc., Crawfordsville, IN, USA) and obtained concentrations of unreacted or free TRITC molecules by comparing them to standard TRITC absorbance with known concentrations. The Beer–Lambert law was applied for this calculation: $[c_1]/[c_2] = OD_1/OD_2$, where c_1 and c_2 are molar concentrations of TRITC solutions with different concentrations, and their optical densities are indicated as OD_1 and OD_2, respectively.

MR Property Characterization of Gd-Mel@SiO_2 NPs

Phantoms were made by various Gd concentrations from 0 to 0.08 mM of Gd-Mel@SiO_2 NPs; Gd-content was measured with ICP-MS, prior to preparation of phantoms. The Gd-Mel@SiO_2 NPs were suspended in 1% agar phantoms and pipetted into microtubes. T_1 and T_2 relaxation times of Magnevist (Gd-DTPA), Gd-Mel NP, and Gd-Mel@SiO_2 NPs were determined using a 7 T MRI scanner (BioSpec, Bruker, Billerica, MA, USA). T_1 was

measured using a gradient-echo sequence with different flip angle (FA = 5–30°) in the same TR = 36 ms and TE = 2.64 ms. T_1 measurements were performed using a nonlinear fit to change in the mean signal intensity of each sample as a function of FA. The r_1 relaxivity values were determined through the curve fitting of relaxation rate $R_1(s^{-1})$ versus the Gd component concentration (mM) (Origin 8). For transversal relaxivity, r_2, a Carr–Purcell–Meiboom– Gill (CPMG) sequence of 6 echos was used with TR = 1000 ms and TE = 9.7–19.4 ms with an echo interval of 9.7 ms. The T_2 values were obtained using a least-squares single exponential R_2 fitting model in pixel by pixel, which averaging over the ROIs. For each concentration, we performed a linear fit between T_2 relaxation values and Gd concentrations with corresponding slope, thus providing r_2 relaxivity (Origin 8).

Cell Culture

A human prostate cancer cell line (PC-3, Manassas, VA, USA) was cultured in standard RPMI 1640 media with 10% fetal bovine serum (FBS) and supplemented with 1% penicillin at 37 °C, under 5% CO_2.

In Vitro Cytotoxicity Evaluation of Gd-Mel@SiO_2 NPs

One-hundred microliters of PC-3 cells with the concentration of 4×10^4/mL were plated on each well of a 96-well plate and incubated for 12 h. Twenty microliters of TRITC-labeled Gd-Mel NP and TRITC-labeled Gd-Mel@SiO_2 NPs were added with the concentrations of 0 to 600 μg/mL and incubated for 4 h. We replaced nanoparticle contained media with fresh cell culturing medium, RPMI to remove free Gd-Mel NP or Gd-Mel@SiO_2 NPs which were not internalized into cells. Then, 10 μL of CCK-8 solution was added into each well to evaluate cell viability and incubated with cells for 2 h before measuring absorbance at 405 nm with a plate reader (Microplate reader SpectraMax M5, Molecular devices, Sunnyvale, CA, USA).

In Vitro Cell Imaging

To measure cellular uptake of TRITC-labeled Gd-Mel@SiO_2 NPs, we plated PC-3 cells for 5×10^5/mL on a round cover glass within a 6 well-plate. The 200 μL of 200 μg/mL TRITC-labeled Gd-Mel@SiO_2 NPs were treated to the cells that were incubated for 4 h. Cell culture medium containing free TRITC-labeled Gd-Mel@SiO_2 NPs was removed from a well, which followed washing steps with PBS buffer. The cells were then fixed with 4% formalin solution and nuclei were stained with 300 μL of 400 nM DAPI. A round cover glass with cells on top was transferred onto slide glass with antifade reagent (Prolong Gold Antifade Mountant, Thermo Fisher Scientific, Waltham, MA, USA). Finally, cells stained with DAPI and incubated with TRITC-labeled Gd-Mel@SiO_2 NPs were analyzed with confocal laser scanning microscopy (CLSM, C2+, Nikon, Minato, Japan) using laser lines of 405 and 543 nm.

In Vitro Assessment of Gd-Mel@SiO_2 NP-mediated Photothermal Therapy

PC-3 cells (4×10^4) were placed on every other well in the middle line of a 96-well plate and treated with 20 μL of one concentration of TRITC-labeled Gd-Mel@SiO_2 NPs and one power density of irradiation. We treated four different concentrations of NPs with 0, 2.4, 12,

and 60 μg/mL. For the condition of one concentration of NPs, four well-plates were prepared to give four different power densities of irradiation: 0, 188, 294, and 464 mW/cm^2. After allowing 4 h for cellular uptake, cells were washed with PBS and the new media was filled. Then, cells were exposed with a laser for 3 min. A single laser probe was manually aligned at 1 cm distance from the bottom of the well and cells were treated with a laser one-by-one in each well-plate. After exposure, the cells were returned to a 37 °C incubator for another 24 h before cell viability tests. Then, a cell viability test using CCK-8 was carried out to determine the relative viabilities in each treated group. The cell viability was calculated based on the total viable PC-3 cells after treatment, relative to the control group without TRITC-labeled Gd-Mel@SiO_2 NPs and a laser. Each sample was counted in triplicate.

In Vivo Assessment of MRI and Fluorescent Imaging Guidance and Photothermal Therapy

TRITC-labeled Gd-Mel@ SiO_2 NPs were applied in an animal model; xenograft mice model with human prostate cancer cells (PC-3) was created by right flank injection which was approved by IACUC in northwestern university. 2–3 weeks old immune compromised CB17-Prkd c SCID/J mice ($n = 6$) were subcutaneously injected with 100 μL of PC-3 cells (2×10^5) suspended in RPMI media. Two weeks were allowed for tumor growth (0.5–1 cm diameter). 10 μL of TRITC-labeled Gd-Mel@SiO_2 NPs in saline at a concentration of 100 μg/mL was inoculated with intratumoral injections. Then, the distribution of TRITC-labeled Gd-Mel@SiO_2 NPs in tumor regions was imaged with OV100 small animal imaging system (Olympus, Tokyo, Japan). Fluorescent image process was conducted with Image-Pro Plus software. In addition, T_1-weighted images were collected to confirm the distribution of TRITC-labeled Gd-Mel@SiO_2 NPs. Mice were anesthetized with isoflurane (mixture of 5% isoflurane and oxygen at 2 L/min), maintaining a physiologic temperature of 37 °C during imaging. MR scans were performed in both coronal and transversal orientations using a spin– echo sequence with following parameters: TR/TE = 500/11.10 ms, flip angle 180°, 1 mm slice thickness, and respiratory triggering with MRI-compatible small animal gating system (model 1025, SA Instruments, Stony Brook, NY, USA). In vivo CNR was calculated by obtaining image contrast between Gd-Mel@SiO_2 NP accumulated region and tumor region, which were estimated by signal-to-noise ratio (SNR) with the equation, $CNR = SNR_{\text{Gd–Mel@SiO2}} - SNR_{\text{tumor}}$. We reconstructed 3D views by combining slices from transverse MR images of mice with ROIs determined by T_1 contrast intensity above 245 by using Jim 6 (Xinapse systems). For the photothermal ablation with TRITC-labeled Gd-Mel@SiO_2 NPs, experimental lasing and heating of the tumor was performed using an 808 nm laser with the optical fiber tip directed toward the center of the tumor and placed 1 cm away from the tumor's surface. The lasing outputs were set to 187.6 mW/cm^2, with continuous lasing for 3 min. During photothermal treatment, real-time thermal imaging of the tumor was performed using an IR thermal camera (ICI7320P, Beaumont, TX, USA).

Histology and Immunohistochemistry

To investigate the efficacy of photothermal ablation with TRITC-labeled Gd-Mel@ SiO_2 NPs, tumors, harvested from mice after ablation therapy were sliced with microtome sectioning. Five-micrometer slices through the center of each tumor were used for staining with hematoxylin and eosin (H&E), terminal deoxynucleotidyl transferase-mediated dUTP

nick end labeling (TUNEL), and heat-shock protein 70 (HSP 70). All slides were analyzed with a TissueFAXS microscope (TissueGnostics GmbH, Vienna, Austria).

RESULTS AND DISCUSSION

Synthesis of Gd-Mel NPs

Mel NP derived from dopamine was synthesized with an oxidative polymerization method modified from the previously reported.[37] Dopamine underwent oxidative polymerization in the presence of sodium hydroxide which initiated the reaction by depriving electrons from amine groups in dopamine molecules.[6] Generation of Mel NP during the polymerization was observed with the immediate color change of solution from transparent to brown. After the reaction, monodispersed Mel NPs with a diameter of 100 nm were observed with transmission electron microscopy (TEM) images (Figure 2a and Figure S1). The yield of Mel NPs in this reaction was approximately 32 wt %, when 150 mg of dopamine hydroxide precursor was used.

Synthesized Mel NP was then doped with paramagnetic gadolinium (Gd) by immersing a Mel NP suspension into the solution of Gd^{3+} for Gd chelated Mel NP. During the electron exchange between quinone and hydroquinone residues,[39] added Gd^{3+} ions in the solution were easily chelated with the quinone molecules and at the same time, protons H^+ were generated as a byproduct during the chelating reaction of $Gd^{3+} + 3/2(2e^- + 2H^+) \rightleftarrows Gd + 3H^+$ (Figure 2b, c). Time dependent change of proton concentration, ($[H^+]$) in the solution during the reaction estimated Gd chelation kinetics (Figure 2c and Figure S2a). Initial Gd chelation rate was obtained from the slope of generated H^+ curves in Figure 2c: initial chelation rate was denoted as $d[H^+]/dt|_{t=0}$, where t is chelation time. When the highest amount of feeding, $[Gd^{3+}] = 879\ \mu M$ was used in the reaction, the fastest initial chelation rate was observed, which was 13.3-fold higher than that in $[Gd^{3+}] = 175\ \mu M$. Considering both $d[H^+]/dt|_{t=0}$ and Gd saturation point which was quantified by inductively coupled plasma mass spectrometry (ICP-MS) Gd elemental analysis, there is a linear decrease trend between $d[Gd]/dt|_{t=0}$ and $[Gd]/[H^+]$ (S2 in SI and Figure S2b). Various amounts of Gd^{3+} from 175 to 1050 μM, those corresponding to 0 to 60% of molar concentration of melanin units, were added to solutions of Mel NPs. Chelated concentration of Gd ([Gd]) tended to linearly increase as addition of $[Gd^{3+}]$ until the saturation point (Figure 2d). The saturated chelation capacity of Mel NPs at the feeding of 879 μM Gd^{3+} was 5.5-fold higher than that of Mel NPs at 175 μM of Gd^{3+} feeding. The calculated average ratio of saturated Gd chelation amounts (32 μM) and monomer of Mel NPs was 1:53 (Gd:monomer of Mel NP) (Figure S2c). Chelation efficiency, $[Gd]/[Gd^{3+}]$ showed gradual decreasing trend after the highest chelation efficiency of 5.4% at $[Gd^{3+}] = 350\ \mu M$ (Figure 2e).

Considering the correlation between proton concentration and Gd chelating kinetics, initial pH condition of the solution was also critical to control Gd chelation in Mel NP. The time dependent Gd chelation was observed at various initial pH conditions of 2, 7, and 9.5. Alkaline condition of pH 9.5 could chelate the highest amount of [Gd] (Figure 2f). Gd chelation efficiency in pH 9.5 was 647-fold and 10.6-fold higher than those at pH 2 and pH 7 solution, respectively (Figure 2g). However, further pH increase of solution higher than pH10.5 degraded Gd-Mel NPs (Figure 2h). Reflecting the optimized chelating conditions of

Mel NPs, we utilized Mel NPs chelated with the feeding [Gd^{3+}] = 1000 μM above the saturated feeding [Gd^{3+}] = 879 μM with an alkaline condition at pH 9.5 to maximize Gd contents in Mel NP for MRI imaging enhancement.

Silica Nanocoating of Gd-Mel NP (Gd-Mel@SiO_2 NP)

After optimizing Gd chelation in Mel NP, controlled formation of silica nanocoating on Mel NP was conducted by hydrolysis and condensation of tetraethyl orthosilicate (TEOS) on cetyltrimethylammonium bromide (CTAB) substrate. CTAB played a crucial role to bind silane precursor[40,41] to Mel NP in the reaction thereby, prevented self-nucleation of silica (Figure S3). The amount of silica nanocoating could be adjusted by the molar ratio of water and TEOS in hydrolysis and condensation sol–gel reaction. When the molar ratio of water and TEOS was 1.77, CTAB molecules with the length of approximately 2.2 nm[42] were initially attached to Mel NP and a ultrathin silica nanoshell (~2 nm) was covered (Gd-Mel@SiO_2-1) (Figure 3a). As increasing molar ratio of water and TEOS, silica nanocoating was initially sparsely grown on the surfaces of Gd-Mel NP (Gd-Mel@SiO_2-1), and then ended up being merged each other and coated the whole surfaces of Gd-Mel NP (Gd-Mel@SiO_2-2 and 3) (Figure 3a). As molar ratio of water and TEOS increased from 0 (bare Mel NP) to 5.525, we observed the size growth up to 1.2 times (from ~99 nm of bare Mel NP to 117 nm of Gd-Mel@SiO_2-3 with average diameter) (Figure 3b). During the reaction, silane precursors were added dropwise slowly with a controlled feeding rate (100 μL/h) to induce slow reaction, which reduced self-nucleation and growth in the form of free silica particles. Silica nanocoating enhanced dispersity of Gd-Mel NP. The zetapotential value of Gd-Mel NP (+22 mV) was significantly decreased to −44.9 mV after silica coating (Gd-Mel@SiO_2-2) (Figure S4). Subsequent amine functionalization of the Gd-Mel@SiO_2-2 with (3-aminopropyl)triethoxysilane (APTES) was also confirmed with the strong positive charge (+31.5 mV) conversion (Figure S4).

Gd and Si elemental mapping images of Gd-Mel@SiO_2 NPs clearly verified silica nanocoating on the Gd-Mel NP. Sparse Si signal was shown as covering spherical Mel NP and chelated Gd element in Mel NP was densely detected in the core region of Gd-Mel@SiO_2 (Figure 3c). The silica nanocoating was further confirmed by dissolving core Gd-Mel NP using hydrogen peroxide (H_2O_2).[5,43] The silica nanocoating layer of Gd-Mel@SiO_2 NPs after etching Gd-Mel NP was clearly appeared with enhanced contrast in comparative TEM images of pre and post H_2O_2 treatment (Figure S5).

Fluorescent Labeling of Gd-Mel@SiO_2 NPs

Amine-terminated Gd-Mel@SiO_2 NPs were labeled with fluorescent dye molecules for an imaging application. It has been known that plenty of quinone residues on the surface of Mel NPs capture most of excited electrons derived from labeled fluorescent dyes under laser irradiation, which results in fluorescence quenching (Figure 4a).[23,44] The strong quenching effect could be confirmed in our synthesized bare Gd-Mel NP labeled with tetramethylrhodamine (TRITC) molecules (Figure 4b). As increasing silica nanocoating thicknesses on Gd-Mel NP, the fluorescent property of TRITC was significantly enhanced (Figure 4b). To quantify enhanced fluorescent efficiency in different thickness of silica nanocoating, we optimized initial feeding amounts of TRITC molecules in conjugation.

When 3 μM solution of TRITC molecules were added to 4 different samples (bare Gd-Mel NPs, Gd-Mel@SiO_2-1, Gd-Mel@SiO_2-2, and Gd-Mel@SiO_2-3), the equivalent amount (1 μM) of TRITC was bound on surfaces of the samples (Figure S6). The identically matched amount of TRITC allowed comparison of fluorescent intensity on the samples. Fluorescent spectra of TRITC-Gd-Mel@SiO_2 NP (1 μM TRITC) with various amounts of silica nanocoating showed an emission peak at wavelength of 569 nm, whereas free TRITC molecules represented an emission at 607 nm during exposure of excitation wavelength at 532 nm (Figure 4c). Emission of all samples were blue-shifted for 38 nm from that of free dyes. The shift of emission is common phenomenon when dye molecules are labeled on or incorporated with NPs.[45,46] The enhanced fluorescent intensities of Gd-Mel@SiO_2-1, 2, 3 were measured as gradually increased 7, 15, and 30 times higher fluorescent than that of bare Gd-Mel NP (Figure 4d). The same fluorescent enhancement with silica nanocoating was further confirmed with fluorescein isothiocyanate (FITC; ex/em = 483/530) having different excitation/emission range with TRITC (ex/em = 532/569) (Figure S7).

MR Imaging Properties of Gd-Mel@SiO_2 NPs

Paramagnetic property of Gd-Mel@SiO_2 NPs for MRI application was first confirmed with a linearly increased magnetization curve upon magnetic field application (Figure 4e). The spin– lattice MRI T_1 contrast effect of our paramagnetic Gd-mel@ SiO_2 NPs was evaluated by comparing the r_1 relaxivity with a clinical grade Gd based T_1 contrast agents, gadopentetate dimeglumine (Gd-DTPA (Gd-diethylenetriaminepentacetate), Magnevist; Schering AG, Berlin, Germany) in 7T MRI. The T_1 positive contrast signal of Gd-Mel NP was stronger than those of Gd-Mel or Gd-DTPA at the same concentration (Figure 4f). The measured spin–lattice r_1 relaxivities in Gd-Mel@SiO_2 NPs, Gd-Mel NP, and Gd-DTPA were 14.3, 4.2, and 0.9 mM^{-1} s^{-1}, respectively (Figure 4g). Noticeably, the r_1 of Gd chelated in Mel NP (Gd-Mel NP) was 4.6 fold higher than Gd chelated in DTPA (Gd-DTPA). The enhanced T_1 contrast effects in Gd-Mel NP could be attributed by the additional innate paramagnetic property of melanin matrices in Gd-Mel NP.[10,47] By the silica nanocoating on Gd-Mel NP, the r_1 relaxivity was further enhanced ~3.4 fold higher than bare Gd-Mel NP with the outer-sphere mechanisms as described in previous reports.[48–50] The more restricted mobility of water diffusion in silica nanocoating led to increased correlation diffusion time of water molecules resulting increased r_1 relaxivity (Figure 4h).[50–52] Dominant contribution of outer-sphere mechanism with silica nanocoating was also evidenced by no significant change of r_2 relaxivities of Gd-Mel NPs and Gd-Mel@SiO_2 NPs, those of 133.15 and 133.17 mM^{-1} s^{-1}, respectively (Figure S8).[50,52–54]

Therapeutic Heat Transduction of Gd-Mel@SiO_2 NPs

Mel NP naturally absorbs light throughout spectral energy, which is mainly due to electric effect of heterogeneous macromolecules of melanin structures.[2] Light absorbed Mel NP exhibits thermal relaxation dominant light energy transfer with nonradiative manners.[2,55] This property becomes a powerful tool in therapeutic perspectives, leading to efficient heat generation for ablating tumors with NIR lasers that can penetrate tissues composed of water and blood by relatively low optical attenuation, “tissue therapeutic window”.[56] The light induced heating property of Gd-Mel@SiO_2 NPs was verified in various concentrations of sample and powers of light (NIR 808 nm). The highest temperature reached up to

sufficiently cytotoxic 57 °C with 1.2 mg/mL of Gd-Mel@SiO_2 in an aqueous solution[57] (Figure 5a) and the heating rate was strongly dependent on the concentration of Gd-Mel@SiO_2 NPs (Figure S9a). The initial heating rate (<100 s) was easily controllable from 0.12–0.22 °C/sec by changing the power of NIR light (187.6–463.7 mW/cm^2) (Figure 5b). A heat transduction efficiency of Gd-Mel@SiO_2 NPs was measured to be 53% using the energy balance equation and time dependent cooling curve (Figure S9b). The resulted heat transduction efficiency was relatively higher than other photothermal metal agents such as gold nanoshells (25%),[38] gold nanorods (50%),[38] iron–platinum nanoparticles (30%).[58] We also clarify the effect of silica nanocoating on photoheat transduction by monitoring time-dependent heating curves of both Gd-Mel NP and Gd-Mel@SiO_2 NPs. As the shallow thickness of silica nanocoating does not affect the photoheat properties, there was no significant difference of photoheating between Gd-Mel NP and Gd-Mel@SiO_2 NPs solutions in various concentrations (Figure S9c, d). Furthermore, Gd-leaching was negligible during laser exposure in both Gd-Mel NPs and Gd-Mel@SiO_2 NPs (Figure S10).

In Vitro Evaluation of Biocompatibility, Fluorescent Imaging, and Therapeutic Properties of Gd-Mel@SiO_2 NPs

The biocompatibility of Gd-Mel@SiO_2 NP was then evaluated with coincubating samples and human prostate cancer cell line (PC-3). The cell cytotoxicity of Gd-Mel@SiO_2 NP and Gd-Mel NP was measured in PC-3 cells after exposure to these samples across the concentrations ranging from 0 to 100 μg/mL. Gd-Mel@SiO_2 NPs showed much lower toxicity showing 70% cell viability at 100 μg/mL, compared to Gd-Mel NP (51% at 100 μg/mL) (Figure 5c). Bioinert silica nanocoating on Gd-Mel NP minimized direct exposure of highly reactive Mel NP to cells, which reduced cell-toxicity. Then, in vitro fluorescent imaging property of the TRITC-Gd-Mel@SiO_2 was tested in PC-3 cells. When the TRITC-Gd-Mel@SiO_2 NP (3.33 μg/mL; nontoxic range) was incubated with PC-3 cells, the TRITC-Gd-Mel@SiO_2 NP binding on cells was well-visualized with red fluorescence (Figure 5d).

In vitro photoheating therapeutic efficacy of Gd-Mel@SiO_2 NPs was subsequently investigated in PC-3 cells treated with four different doses (0, 0.4, 2, and 10 μg/mL) of Gd-Mel@SiO_2 NPs and irradiating an NIR light (within safe laser power range; Maximum Permissible Exposure (MPE) of skin: < 0.5 mW/cm^2).[20] The PC-3 cancer cell death was effectively achieved by controlling the concentration of Gd-Mel@SiO_2 NPs and applied power of NIR light. The cells treated with Gd-Mel@ SiO_2 NPs above 2 μg/mL and NIR irradiations (188, 294, and 464 mW/cm^2) for 5 min exhibited significant cell death. The PC-3 cancer cells treated with Gd-Mel@SiO_2 NPs in concentration of 10 μg/mL and irradiating NIR light of 464 mW/cm^2 showed 58% suppressed cell viability comparing with nontreated or only NIR treated cells (Figure 5e).

In Vivo Feasibility Study of Multimodal Image-Guidance and Therapeutic Application of Gd-Mel@ SiO_2 NPs

Our Gd-Mel@SiO_2 NPs optimized with combinations of paramagnetic Gd, Mel NPs and silica nanocoating can be utilized for *in vivo* dual-modal contrast enhanced MRI/fluorescent imaging. The dual modal MRI/fluorescent imaging technique combining MRI having high spatial resolution and fluorescent imaging enabling the real-time navigation has been

performed for a precise imaging-guided therapies. Their contrast enhancement agents will provide a new direction for minimally- or noninvasive interventional cancer therapy by ensuring more selective delineate the tumor or disease and precise delivery of therapeutics without damaging surrounding normal tissues.[59,60] Our optimized Gd-Mel@SiO_2-3 (about ~18 nm Silica shell) preventing fluorescent dye quenching and enhancing MR contrast by outer sphere model was selected to test Gd-Mel@SiO_2 NPs as a potential nanoagent for the in vivo dual-modal MRI/fluorescent contrast enhancement. PC-3 prostate tumor-bearing mice were generated and scanned with MRI to confirm the tumor site and volume before injection of Gd-Mel@SiO_2 NPs (Figure 6a). After ensuring tumor mass and injection site in MR T_1 scanning (Figure 6a, c), TRITC-Gd-Mel@SiO_2 NPs (10 μg) were injected to the center of PC-3 prostate tumor in mice via catheter directed intratumoral injection. The distribution of infused TRITC-Gd-Mel@SiO_2 NPs in tumors could be monitored with both MRI T_1 weighted images and fluorescent images (Figure 6a, b). The transversal MR T_1-weighted images in Figure 6a exhibited clear deposition of Gd-Mel@SiO_2 NPs. Contrast to noise ratios (CNR) of pre- and postinjected tumors confirmed significant increase of 9.3 times after injection of Gd-Mel@SiO_2 NPs (Figure 6a). The infused TRITC-Gd-Mel@SiO_2 NPs with MR image guidance in a tumor were also exhibited strong red fluorescence in the in vivo fluorescent imaging system (Figure 6b). A target to background ratio (TBR) from Gd-Mel@SiO_2 NP-accumulated region was 14.3 times higher than that from normal tissue. Further, three-dimensional (3D) reconstruction of MR coronal images enables monitoring injection trajectory and infused Gd-Mel@SiO_2 NPs in ROI where brighter T_1 intensity value was above 245. Those MR images could be coregistered with the fluorescent images which permit finding the key therapeutic spots such as focusing laser or resections. As 3D accumulated region of Gd-Mel@SiO_2 NPs was projected to two-dimensional (2D) ROI of fluorescent image, the shape of Gd-Mel@SiO_2 deposition showed consistency in both images. Furthermore, estimated volume of deposition obtained from MR 3D reconstructed images was 16.2 mm^3 which was comparable to 21.5 mm^3, estimated with fluorescent images where the diameter of accumulation was 3.45 mm (Figure 6b, c). These in vivo dual-modal imaging-guidance process could be achieved with our TRITC-Gd-Mel@SiO_2 contrast enhancement agents and it should be useful for adjusting position of catheter, delineating tumors, intraoperative imaging and minimally invasive cancer therapeutics. The IT infused TRITC-labeled Gd-Mel@SiO_2 NPs were well-retained with high CNR ratio in the tumor injection site for 24 h, as confirmed in multimodal imaging. Comprehensive biodistribution studies showing the Gd-Mel@SiO_2 NPs amounts in each organ will be warranted for further preclinical imaging and therapeutic applications.

As ensured the focusing NIR light spot (~20 mm diameter) where targeted Gd-Mel@SiO_2 NPs with multimodal MR and fluorescent imaging, we performed NIR light irradiation (187.6 mW/cm^2) for photoheating cancer therapy, while monitoring temperature elevation of tumors using IR thermal camera. Temperature was rapidly increased over NIR light irradiated region, reaching up to 60 °C in 2 min. The highest temperature of 63 °C covering the whole tumor region above 50 °C was achieved (Figure 6d). The treated lesions with Gd-Mel@SiO_2 NPs and NIR light showed significant necrotic shrinkage of cells and eruption of extracellular matrix, thus contacted viable cells were hardly observable in the tumor stained with Hematoxylin and Eosin (H&E) (Figure 6e). Significant apoptotic cancer cell death was

also observed throughout the tumor tissues (Figure 6e). The TRITC-Gd-Mel@SiO_2 NPs mediated photoheating cancer cell damages in the tumor regions were further confirmed with significant expression of heat-shock protein 70 (HSP 70) that is a biological marker of stimulated immune response by heat-stress[61–63] (Figure 6e).

CONCLUSIONS

In conclusion, we designed and synthesized Gd-Mel@SiO_2 NP to fully utilize advantageous properties of Mel NPs for the dual-modal contrast enhanced MRI/fluorescent imaging. The highly efficient Gd chelation on Mel NP could be optimized by adjusting feeding amounts of Gd^{3+} ions and pH of the solution. The Gd-Mel NP was successfully coated with a controlled silica layer. The silica nanocoating on Gd-Mel NP (Gd-Mel@SiO_2 NP) significantly prevented fluorescent quenching and demonstrated the strong fluorescent intensity of labeled TRITC. The MR r_1 relaxivity of Gd-Mel NP was also greatly improved by the silica nanocoating. Further, high heat transduction efficiency (~53%) and sufficient tumorcidal heating of Gd-Mel@SiO_2 NPs were demonstrated. The TRITC-Gd-Mel@SiO_2 NPs allowed in vivo dual-modal contrast enhanced MR and fluorescent imaging and image-guided catheter-directed infusion for photoheating cancer therapy in clinically relevant human prostate cancer xenograft mouse model. As emphasized importance and high demand for the development of multimodal imaging contrast enhancement agents in the current minimal- or noninvasive cancer therapeutics, the developed Gd-Mel@SiO_2 NPs represent a promising diagnostic and intraoperative contrast enhancement imaging and therapeutic agent for the treatment of various cancers.

Acknowledgments

This work was supported by four grants R01CA141047, R21CA173491, R21EB017986, and R21CA185274 from the National Cancer Institute and National Institute of Biomedical Imaging and Bioengineering. This work was also supported by the Center for Translational Imaging and Mouse Histology and Phenotyping Laboratory at Northwestern University. All authors are grateful to Eric W. Roth (NUANCE/QBIC, Northwestern University) for the support of STEM analysis and Prof. Andrew C. Larson (Department of Radiology, Northwestern University) for generous discussion on MR images, and Dr. Xiaoke Huang (Department of Radiology, Northwestern University) for providing PC-3 cells.

References

1. Brenner M, Hearing VJ. The Protective Role of Melanin Against UV Damage in Human Skin. Photochem Photobiol. 2008; 84:539–549. [PubMed: 18435612]
2. Meredith P, Powell BJ, Riesz J, Nighswander-Rempel SP, Pederson MR, Moore EG. Towards Structure-Property-Function Relationships for Eumelanin. Soft Matter. 2006; 2:37–44.
3. Miao Z-H, Wang H, Yang H, Li Z-L, Zhen L, Xu C-Y. Intrinsically Mn^{2+}-Chelated Polydopamine Nanoparticles for Simultaneous Magnetic Resonance Imaging and Photothermal Ablation of Cancer Cells. ACS Appl Mater Interfaces. 2015; 7:16946–16952. [PubMed: 26196160]
4. Dadachova E, Bryan RA, Howell RC, Schweitzer AD, Aisen P, Nosanchuk JD, Casadevall A. The Radioprotective Properties of Fungal Melanin Are a Function of Its Chemical Composition, Stable Radical Presence and Spatial Arrangement. Pigm Cell Melanoma Res. 2008; 21:192–199.
5. Ito S, Wakamatsu K. Chemical Degradation of Melanins: Application to Identification of Dopamine-Melanin. Pigm Cell Res. 1998; 11:120–126.
6. Ju KY, Lee Y, Lee S, Park SB, Lee JK. Bioinspired Polymerization of Dopamine to Generate Melanin-Like Nanoparticles Having an Excellent Free-Radical-Scavenging Property. Biomacromolecules. 2011; 12:625–632. [PubMed: 21319809]

7. Riley, PA., Borovansky, J. Melanins and Melanosomes: Biosynthesis, Biogenesis, Physiological, and Pathological Functions. Wiley-Blackwell; Hoboken, NJ: 2011. p. 15-17.
8. Liu YL, Ai KL, Liu JH, Deng M, He YY, Lu LH. Dopamine-Melanin Colloidal Nanospheres: An Efficient Near-Infrared Photothermal Therapeutic Agent for *In Vivo* Cancer Therapy. Adv Mater. 2013; 25:1353–1359. [PubMed: 23280690]
9. Wang XY, Zhang JS, Wang YT, Wang CP, Xiao JR, Zhang Q, Cheng YY. Multi-Responsive Photothermal-Chemotherapy with Drug-Loaded Melanin-Like Nanoparticles for Synergetic Tumor Ablation. Biomaterials. 2016; 81:114–124. [PubMed: 26731575]
10. Enochs WS, Petherick P, Bogdanova A, Mohr U, Weissleder R. Paramagnetic Metal Scavenging by Melanin: MR Imaging. Radiology. 1997; 204:417–423. [PubMed: 9240529]
11. Felix CC, Hyde JS, Sarna T, Sealy RC. Interactions of Melanin with Metal-Ions - Electron-Spin Resonance Evidence for Chelate Complexes of Metal-Ions with Free-Radicals. J Am Chem Soc. 1978; 100:3922–3926.
12. Morlieras J, Chezal J-M, Miot-Noirault E, Roux A, Heinrich-Balard L, Cohen R, Tarrit S, Truillet C, Mignot A, Hachani R, Kryza D, Antoine R, Dugourd P, Perriat P, Janier M, Sancey L, Lux F, Tillement O. Development of Gadolinium Based Nanoparticles Having an Affinity towards Melanin. Nanoscale. 2013; 5:1603–1615. [PubMed: 23334308]
13. Godechal Q, Mignion L, Karroum O, Magat J, Danhier P, Morandini R, Ghanem GE, Leveque P, Gallez B. Influence of Paramagnetic Melanin on the MRI Contrast in Melanoma: a Combined High-Field (11.7 T) MRI and EPR Study. Contrast Media Mol Imaging. 2014; 9:154–160. [PubMed: 24523060]
14. Ju KY, Lee JW, Im GH, Lee S, Pyo J, Park SB, Lee JH, Lee JK. Bio-Inspired, Melanin-Like Nanoparticles as a Highly Efficient Contrast Agent for T-1-Weighted Magnetic Resonance Imaging. Biomacromolecules. 2013; 14:3491–3497. [PubMed: 23987128]
15. Zhang Y, White SB, Nicolai JR, Zhang ZL, West DL, Kim DH, Goodwin AL, Miller FH, Omary RA, Larson AC. Multimodality Imaging to Assess Immediate Response to Irreversible Electroporation in a Rat Liver Tumor Model. Radiology. 2014; 271:721–729. [PubMed: 24555632]
16. Gordon AC, Lewandowski RJ, Salem R, Day DE, Omary RA, Larson AC. Localized Hyperthermia with Iron Oxide-Doped Yttrium Microparticles: Steps toward Image-Guided Thermoradiotherapy in Liver Cancer. J Vasc Interv Radiol. 2014; 25:397–404. [PubMed: 24315666]
17. Sun J, Teng ZG, Tian Y, Wang JD, Guo Y, Kim DH, Larson AC, Lu GM. Targeted Fluorescent Magnetic Nanoparticles for Imaging of Human Breast Cancer. Int J Clin Exp Med. 2014; 7:4747–4758. [PubMed: 25663971]
18. Wood BJ, Locklin JK, Viswanathan A, Kruecker J, Haemmerich D, Cebral J, Sofer A, Cheng R, McCreedy E, Cleary K, McAuliffe MJ, Glossop N, Yanof J. Technologies for Guidance of Radiofrequency Ablation in the Multimodality Interventional Suite of the Future. J Vasc Interv Radiol. 2007; 18:9–24. [PubMed: 17296700]
19. Elhawary H, Oguro S, Tuncali K, Morrison PR, Tatli S, Shyn PB, Silverman SG, Hata N. Multimodality Non-rigid Image Registration for Planning, Targeting and Monitoring During CT-Guided Percutaneous Liver Tumor Cryoablation. Acad Radiol. 2010; 17:1334–1344. [PubMed: 20817574]
20. Kim DH, Larson AC. Deoxycholate Bile Acid Directed Synthesis of Branched Au Nanostructures for Near Infrared Photothermal Ablation. Biomaterials. 2015; 56:154–164. [PubMed: 25934288]
21. Janjic JM, Srinivas M, Kadayakkara DKK, Ahrens ET. Self-delivering Nanoemulsions for Dual Fluorine-19 MRI and Fluorescence Detection. J Am Chem Soc. 2008; 130:2832–2841. [PubMed: 18266363]
22. Panzella L, Gentile G, D'Errico G, Della Vecchia NF, Errico ME, Napolitano A, Carfagna C, d'Ischia M. Atypical Structural and pi-Electron Features of a Melanin Polymer That Lead to Superior Free-Radical-Scavenging Properties. Angew Chem, Int Ed. 2013; 52:12684–12687.
23. Medintz IL, Stewart MH, Trammell SA, Susumu K, Delehanty JB, Mei BC, Melinger JS, Blanco-Canosa JB, Dawson PE, Mattoussi H. Quantum-Dot/Dopamine Bioconjugates Function as Redox Coupled Assemblies for In Vitro and Intracellular pH Sensing. Nat Mater. 2010; 9:676–684. [PubMed: 20651808]

24. Qiang WB, Li W, Li XQ, Chen X, Xu DK. Bioinspired Polydopamine Nanospheres: a Superquencher for Fluorescence Sensing of Biomolecules. Chem Sci. 2014; 5:3018–3024.
25. Wakamatsu K, Ito S. Advanced Chemical Methods in Melanin Determination. Pigm Cell Res. 2002; 15:174–183.
26. Dreyer DR, Miller DJ, Freeman BD, Paul DR, Bielawski CW. Elucidating the Structure of Poly(dopamine). Langmuir. 2012; 28:6428–6435. [PubMed: 22475082]
27. Liebscher J, Mrowczynski R, Scheidt HA, Filip C, Hadade ND, Turcu R, Bende A, Beck S. Structure of Polydopamine: A Never-Ending Story? Langmuir. 2013; 29:10539–10548. [PubMed: 23875692]
28. Herve M, Hirschinger J, Granger P, Gilard P, Deflandre A, Goetz N. A C-13 Solid-State NMR-Study of the Structure and Autoxidation Process of Natural and Synthetic Melanins. Biochim Biophys Acta, Protein Struct Mol Enzymol. 1994; 1204:19–27.
29. Wang Y, Wang Z, Ma PM, Bai HY, Dong WF, Xie Y, Chen MQ. Strong Nanocomposite Reinforcement Effects in Poly(vinyl alcohol) with Melanin Nanoparticles. RSC Adv. 2015; 5:72691–72698.
30. Han J, Park W, Park SJ, Na K. Photosensitizer-Conjugated Hyaluronic Acid-Shielded Polydopamine Nanoparticles for Targeted Photomediated Tumor Therapy. ACS Appl Mater Interfaces. 2016; 8:7739–7747. [PubMed: 26965036]
31. Thanh NTK, Green LAW. Functionalisation of Nanoparticles for Biomedical Applications. Nano Today. 2010; 5:213–230.
32. Zrazhevskiy P, Sena M, Gao XH. Designing Multifunctional Quantum Dots for Bioimaging, Detection, and Drug Delivery. Chem Soc Rev. 2010; 39:4326–4354. [PubMed: 20697629]
33. Liz-Marzan LM, Mulvaney P. The Assembly of Coated Nanocrystal. J Phys Chem B. 2003; 107:7312–7326.
34. Guerrero-Martinez A, Perez-Juste J, Liz-Marzan LM. Recent Progress on Silica Coating of Nanoparticles and Related Nanomaterials. Adv Mater. 2010; 22:1182–1195. [PubMed: 20437506]
35. Vivero-Escoto JL, Huang YT. Inorganic-Organic Hybrid Nanomaterials for Therapeutic and Diagnostic Imaging Applications. Int J Mol Sci. 2011; 12:3888–3927. [PubMed: 21747714]
36. Tang L, Cheng JJ. Nonporous Silica Nanoparticles for Nanomedicine Application. Nano Today. 2013; 8:290–312. [PubMed: 23997809]
37. Cho S, Kim S-H. Hydroxide Ion-Mediated Synthesis of Monodisperse Dopamine-Melanin Nanospheres. J Colloid Interface Sci. 2015; 458:87–93. [PubMed: 26210098]
38. Pattani VP, Tunnell JW. Nanoparticle-Mediated Photothermal Therapy: A Comparative Study of Heating for Different Particle Types. Lasers Surg Med. 2012; 44:675–684. [PubMed: 22933382]
39. Meredith P, Sarna T. The Physical and Chemical Properties of Eumelanin. Pigm Cell Res. 2006; 19:572–594.
40. Prabhakar N, Nareoja T, von Haartman E, Karaman DS, Jiang H, Koho S, Dolenko TA, Hanninen PE, Vlasov DI, Ralchenko VG, Hosomi S, Vlasov II, Sahlgren C, Rosenholm JM. Core-Shell Designs of Photoluminescent Nanodiamonds with Porous Silica Coatings for Bioimaging and Drug Delivery II: Application. Nanoscale. 2013; 5:3713–22. [PubMed: 23493921]
41. Ho CC, Ding SJ. Dopamine-Induced Silica-Polydopamine Hybrids with Controllable Morphology. Chem Commun. 2014; 50:3602–3605.
42. Mohanty P, Lee J, Glover KJ, Landskron K. Discoid Bicelles as Efficient Templates for Pillared Lamellar Periodic Mesoporous Silicas at pH 7 and Ultrafast Reaction Times. Nanoscale Res Lett. 2010; 6:61. [PubMed: 21711577]
43. Korytowski W, Sarna T. Bleaching of Melanin Pigments - Role of Copper Ions and Hydrogen-Peroxide in Autooxidation and Photooxidation of Synthetic Dopa-Melanin. J Biol Chem. 1990; 265:12410–12416. [PubMed: 2165063]
44. Xiangzhao A, Qiang M, Xingguang S. Nanosensor for Dopamine and Glutathione based on the Quenching and Recovery of the Fluorescence of Silica-Coated Quantum Dots. Microchim Acta. 2013; 180:269–277.
45. Avnir D, Levy D, Reisfeld R. The Nature of the Silica Cage as Reflected by Spectral Changes and Enhanced Photostability of Trapped Rhodamine-6g. J Phys Chem. 1984; 88:5956–5959.

46. Carbonaro CM, Corpino R, Ricci PC, Chiriu D, Cannas C. Fluorescence Properties of Dye Doped Mesoporous Silica. AIP Conf Proc. 2014; 1624:23–30.
47. Atlas SW, Braffman BH, LoBrutto R, Elder DE, Herlyn D. Human Malignant Melanomas with Varying Degrees of Melanin Content in Nude Mice: MR Imaging, Histopathology, and Electron Paramagnetic Resonance. J Comput Assist Tomogr. 1990; 14:547–554. [PubMed: 2164537]
48. Caravan P, Ellison JJ, McMurry TJ, Lauffer RB. Gadolinium(III) Chelates as MRI Contrast Agents: Structure, Dynamics, and Applications. Chem Rev. 1999; 99:2293–2352. [PubMed: 11749483]
49. Werner EJ, Datta A, Jocher CJ, Raymond KN. High-Relaxivity MRI Contrast Agents: Where Coordination Chemistry Meets Medical Imaging. Angew Chem, Int Ed. 2008; 47:8568–8580.
50. Chen F, Bu WB, Zhang SJ, Liu JN, Fan WP, Zhou LP, Peng WJ, Shi JL. Gd^{3+}-Ion-Doped Upconversion Nanoprobes: Relaxivity Mechanism Probing and Sensitivity Optimization. Adv Funct Mater. 2013; 23:298–307.
51. Ananta JS, Godin B, Sethi R, Moriggi L, Liu XW, Serda RE, Krishnamurthy R, Muthupillai R, Bolskar RD, Helm L, Ferrari M, Wilson LJ, Decuzzi P. Geometrical Confinement of Gadolinium-based Contrast Agents in Nanoporous Particles Enhances T-1 Contrast. Nat Nanotechnol. 2010; 5:815–821. [PubMed: 20972435]
52. Carniato F, Tei L, Dastru W, Marchese L, Botta M. Relaxivity Modulation in Gd-Functionalised Mesoporous Silicas. Chem Commun. 2009; 10:1246–1248.
53. Wartenberg N, Fries P, Raccurt O, Guillermo A, Imbert D, Mazzanti M. A Gadolinium Complex Confined in Silica Nanoparticles as a Highly Efficient T1/T2MRI Contrast Agent. Chem - Eur J. 2013; 19:6980–6983. [PubMed: 23606305]
54. Liu JN, Bu WB, Shi JL. Silica Coated Upconversion Nanoparticles: A Versatile Platform for the Development of Efficient Theranostics. Acc Chem Res. 2015; 48:1797–1805. [PubMed: 26057000]
55. Meredith P, Riesz J. Radiative Relaxation Quantum Yields for Synthetic Eumelanin. Photochem Photobiol. 2004; 79:211–216. [PubMed: 15068035]
56. Weissleder R. A Clearer Vision for *In Vivo* Imaging. Nat Biotechnol. 2001; 19:316–317. [PubMed: 11283581]
57. Chu KF, Dupuy DE. Thermal Ablation of Tumours: Biological Mechanisms and Advances in Therapy. Nat Rev Cancer. 2014; 14:199–208. [PubMed: 24561446]
58. Chen C-L, Kuo L-R, Lee S-Y, Hwu Y-K, Chou S-W, Chen C-C, Chang F-H, Lin K-H, Tsai D-H, Chen Y-Y. Photothermal Cancer Therapy via Femtosecond-Laser-Excited FePt Nanoparticles. Biomaterials. 2013; 34:1128–1134. [PubMed: 23137396]
59. Zha Z, Wang J, Qu E, Zhang S, Jin Y, Wang S, Dai Z. Polypyrrole Hollow Microspheres as Echogenic Photothermal Agent for Ultrasound Imaging Guided Tumor Ablation. Sci Rep. 2013; 3:2360. [PubMed: 23912977]
60. Yang K, Hu L, Ma X, Ye S, Cheng L, Shi X, Li C, Li Y, Liu Z. Multimodal Imaging Guided Photothermal Therapy using Functionalized Graphene Nanosheets Anchored with Magnetic Nanoparticles. Adv Mater. 2012; 24:1868–1872. [PubMed: 22378564]
61. Chu KF, Dupuy DE. Thermal Ablation of Tumours: Biological Mechanisms and Advances in Therapy. Nat Rev Cancer. 2014; 14:199–208. [PubMed: 24561446]
62. Schueller G, Kettenbach J, Sedivy R, Stift A, Friedl J, Gnant M, Lammer J. Heat Shock Protein Expression Induced by Percutaneous Radiofrequency Ablation of Hepatocellular Carcinoma *In Vivo*. Int J Oncol. 2004; 24:609–613. [PubMed: 14767545]
63. Teng L-S, Jin K-T, Han N, Cao J. Radiofrequency ablation, heat shock protein 70 and potential anti-tumor immunity in hepatic and pancreatic cancers: a minireview. Hepatobiliary Pancreatic Dis Int. 2010; 9:361–365.

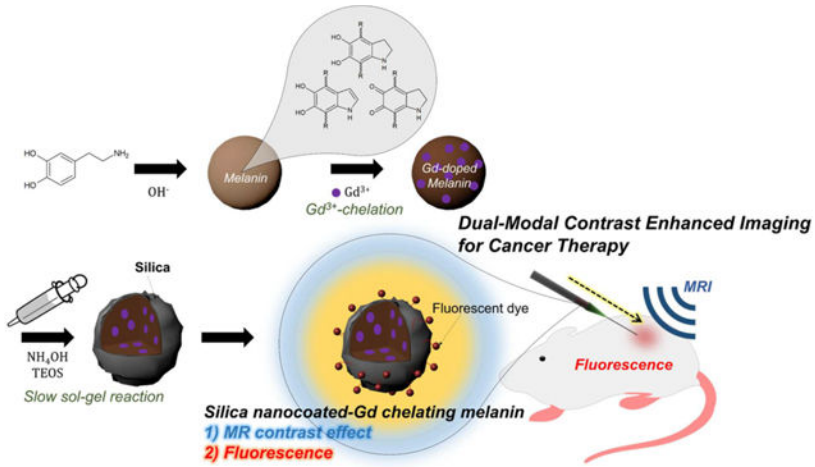

Figure 1.

Illustration of gadolinium chelated melanin nanoparticles with silica nanocoating (Gd-Mel@SiO_2 NPs) in preparation and application. Dopamine molecules start polymerization in the presence of hydroxide ions and end up making spherical melanin nanoparticles (Mel NP). Paramagnetic Gd^{3+} ions are chelated in melanin matrices for MRI T_1 contrast effect. Then, a silica layer is formed on the surfaces of Mel NP with a slow sol–gel reaction controlling a feeding of precursor to reduce self-nucleation of free silica particles. Lastly, fluorescent dye molecules are labeled for the fluorescent imaging of Gd-Mel@SiO_2 NPs without significant electron quenching. Our developed fluorescent dye-labeled Gd-Mel@SiO_2 NPs are applied to dual-modal contrast enhanced MRI/fluorescent image-guidance for cancer therapy.

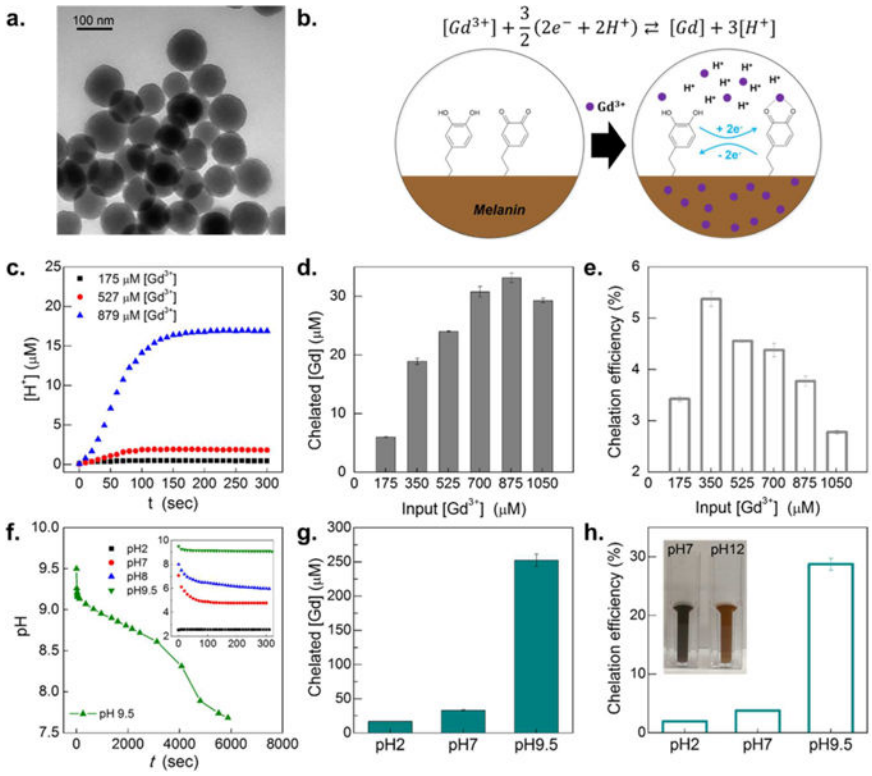

Figure 2.

(a) Transmission electron microscopy (TEM) image of Mel NPs. (b) Illustration of chelation mechanism of gadolinium ions, Gd^{3+} in Mel NP: after introducing Gd^{3+} into suspension, hydroquinone residues in Mel NP undergo electron exchange. Hydroquinone is transformed to quinone by giving off protons but chelating gadolinium ions in the Mel NP matrices. The proton concentration increases until reaching equilibrium. (c) Time dependence of proton concentrations, $[H^+]$, measured after addition of Gd^{3+} ions: three different concentrations of Gd^{3+} ($[Gd^{3+}]$) were used for 175, 527, and 879 μM. The initial solution pH was 7 and suspension concentration of Mel NPs was 400 μg/mL. (d) Chelated gadolinium concentration, [Gd] as a function of added $[Gd^{3+}]$ with Mel NP suspension concentrations of 400 μg/mL. (e) Chelation efficiency (%) as a function of added $[Gd^{3+}]$. (f) Time-dependent pH changes, measured after added 879 μM of Gd^{3+} into a suspension of Mel NP (400 μg/mL), where initial pH was 9.5. The inset indicates time dependence of pH change after added 879 μM of Gd^{3+} into the suspensions of Mel NP, where three initial pH conditions were 2, 7, 8, and 9.5. (g) Initial suspension pH dependence of chelated [Gd], where $[Gd^{3+}]$ was 879 μM in the suspension of Mel NP; three different pH conditions of Mel NP suspensions were 2, 7, and 9.5. (h) Chelation efficiency (%) as a function of initial suspension pH with Mel NP (400 μg/mL), where three different pH conditions were 2, 7, and 9.5. The inset of digital camera image shows suspensions of Gd-chelated melanin nanoparticles (Gd-Mel NP), where the initial pH conditions were 7 and 12, respectively.

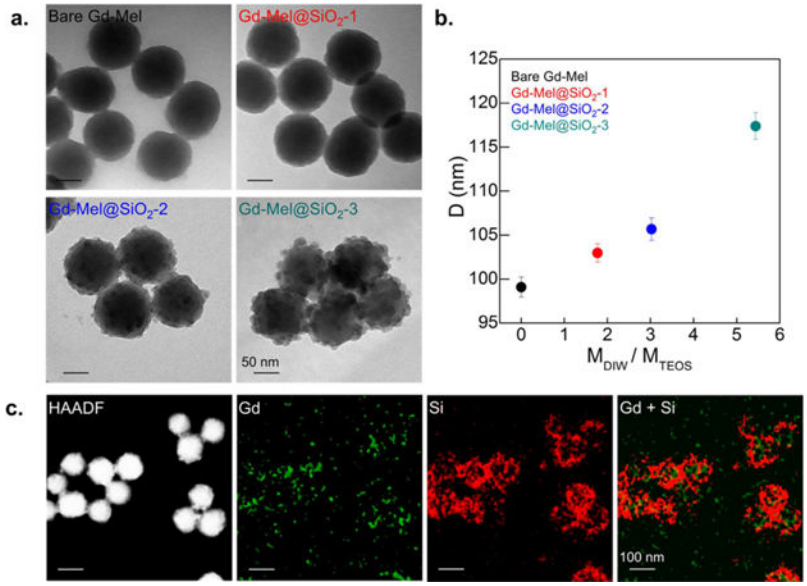

Figure 3.

(a) TEM images of as-synthesized Gd-Mel NP with controlled amount of silica nanocoating: the leftmost image shows bare Gd-Mel NP and rest three TEM images show controlled silica nanocoating on Gd-Mel NPs (Gd-Mel@SiO_2 NPs), indicated as Gd-Mel@SiO_2-1, Gd-Mel@SiO_2-2, and Gd-Mel@SiO_2-3 in each panel. (b) Diameter (D) of Gd-Mel@SiO_2 NPs as a function of molar ratio of distilled water and tetraethyl orthosilicate (TEOS) (M_{DIW}/M_{TEOS}). (c) High-angle annular dark-field scanning transmission electron microscopy (HAADF-STEM) image of Gd-Mel@SiO_2 NPs and elemental mapping images of gadolinium (Gd) and silicon (Si), respectively and their superposition of elemental maps of Gd and Si.

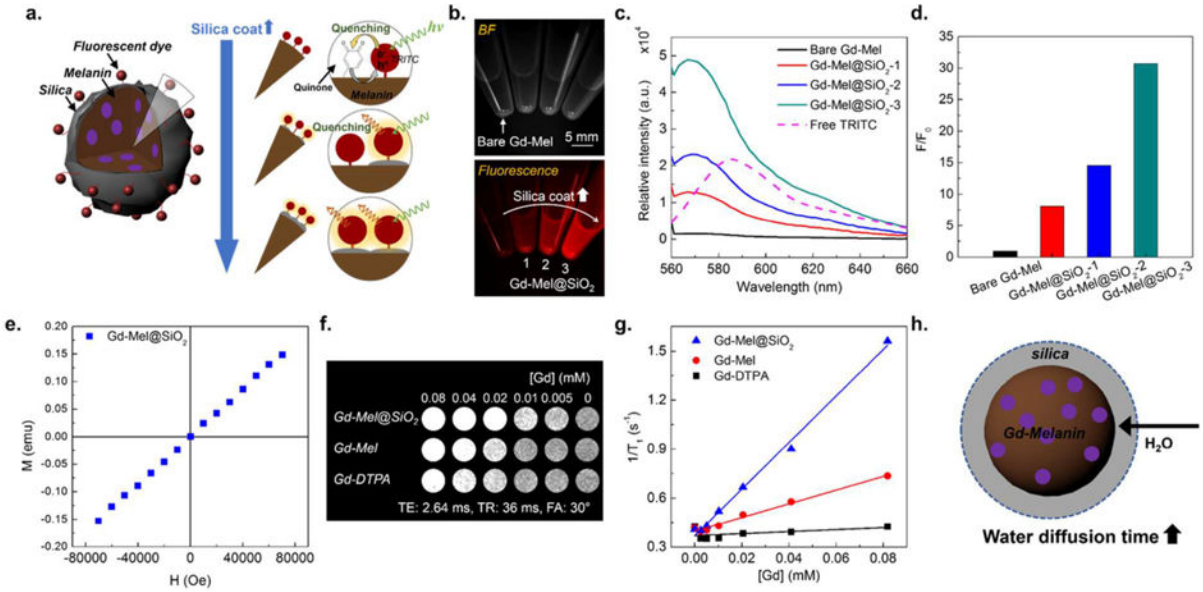

Figure 4.

(a) Illustration of fluorescent property of fluorescent dye-labeled Gd-Mel@SiO_2 NPs: fluorescence quenching occurs in bare Gd-Mel NP, because excited electrons from fluorescent molecules with a laser are captured by quinone residues in melanin. Less contact between melanin and fluorescent molecules by silica nanocoating barriers enhances fluorescent intensity. (b) Bright-field (BF) and fluorescent images of four vials containing tetramethylrhodamine (TRITC)-labeled bare Gd-Mel NPs and TRITC-labeled Gd-Mel@SiO_2 NPs indicated as 1, 2, and 3 that corresponding to Gd-Mel@SiO_2-1, Gd-Mel@SiO_2-2, and Gd-Mel@SiO_2-3, respectively. (c) Fluorescent spectra of 1 μM TRITC-labeled bare Gd-Mel, Gd-Mel@SiO_2-1, Gd-Mel@SiO_2-2, Gd-Mel@SiO_2-3, and 0.66 μM free TRITC molecules, acquired at excitation wavelength of 532 nm. (d) Fluorescence ratio between TRITC-labeled Gd-Mel@SiO_2 NPs and TRITC-labeled Gd-Mel NP. Fluorescent intensity was acquired at 569 nm from fluorescent spectra of bare Gd-Mel, Gd-Mel@SiO_2-1, Gd-Mel@SiO_2-2, and Gd-Mel@SiO_2-3, which were expressed in ratio. (e) A magnetization curve of Gd-Mel@SiO_2 NPs, obtained at 300 K. (f) T_1 weighted images of agarose phantoms containing Gd-Mel@SiO_2 NPs, Gd-Mel NPs, and Gd-DTPA, respectively, where gadolinium concentration ([Gd]) were indicated in a top row. T_1 weighted images were obtained at TE of 2.64 ms, TR of 36 ms, and flip angle (FA) of 30°. (g) T_1 relaxivity depending on [Gd] in Gd-DTPA, Gd-Mel NPs, and Gd-Mel@SiO_2 NPs: r_1 relaxivities are 14.3, 4.2, and 0.9 mM^{-1} s^{-1}, respectively. (h) Illustration of r_1 relaxivity enhancement by increase in water diffusion time in silica shell to Gd-Mel NP.

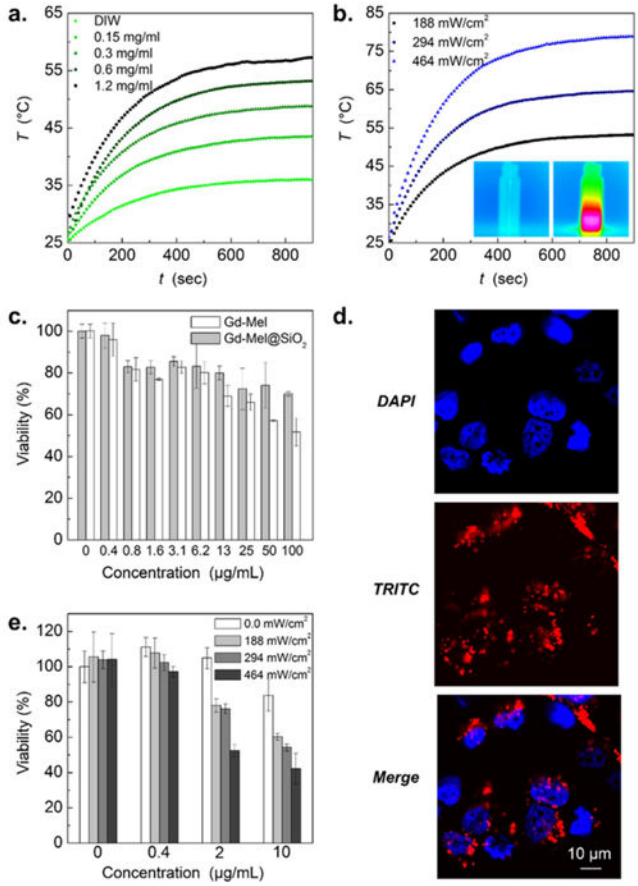

Figure 5.

(a) Time-dependent increase of temperature in solutions of Gd-Mel@SiO_2 NPs with concentrations of 0, 0.15, 0.3, 0.6, and 1.2 mg/mL, respectively, during near-infrared (NIR) radiation (188 mW/cm^2). (b) Time dependent temperature changes of Gd-Mel@SiO_2 NPs solutions with a concentration of 0.3 mg/mL, irradiated with three different powers of 808 nm NIR light (188 mW/cm^2, 294 mW/cm^2, and 464 mW/cm^2), respectively. Insets of temperature mapping images indicate before and after NIR radiation, respectively. (c) Cytotoxicity of TRITC-labeled Gd-Mel NPs and TRITC-labeled Gd-Mel@SiO_2 NPs against human prostate cancer cells (PC-3) with respect to the concentration. (d) Fluorescent images of PC-3 cells, stained with DAPI for nuclei and encapsulating TRITC-labeled Gd-Mel@SiO_2 NPs, and the superposition of DAPI and TRITC, as indicated in each panel. (e) Photoheat treated cell viability depending on the concentration of TRITC-labeled Gd-Mel@SiO_2 NPs (0, 0.4, 2, and 10 μg/mL) and power of NIR light (0, 188, 294, and 464 mW/cm^2).

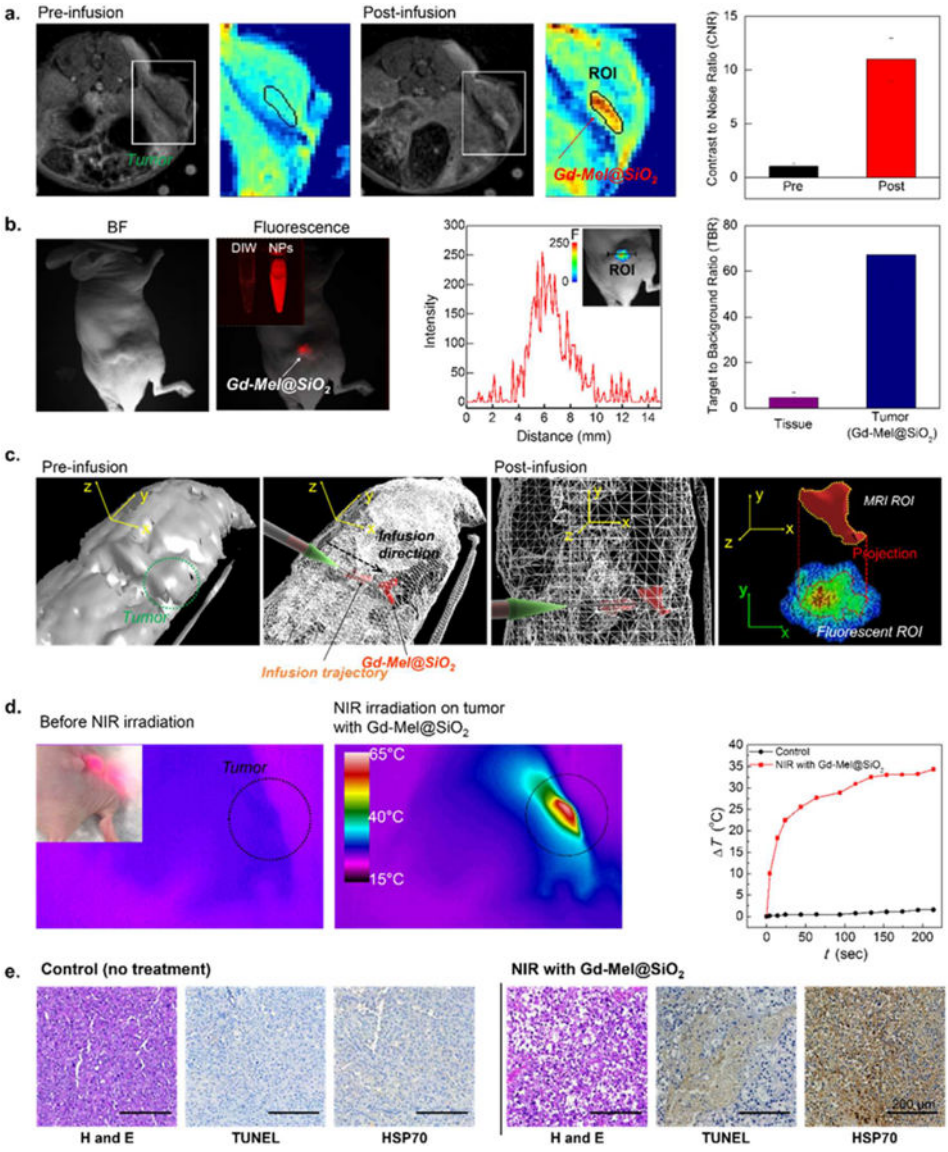

Figure 6.

(a) T_1 MR images of human prostate tumor xenograft mouse at pre- and postinfusion of TRITC-labeled Gd-Mel@SiO_2 NPs, where the area of tumor is indicated with color map images and the region of inoculated TRITC-labeled Gd-Mel@SiO_2 NPs is indicated with red color. Contrast to noise ratio (CNR) in the region of interest (ROI), indicated in the MR color map images with black lines from a pre- and postinjected tumor. (b) (b, left) BF and fluorescent images of the mouse after injection of TRITC-labeled Gd-Mel@SiO_2 NPs, as indicated in each panel. The inset image shows vials with distilled water and solution containing TRITC-labeled Gd-Mel@SiO_2 NPs. (b, center) Line scan of fluorescent intensity in the tumor with TRITC-labeled Gd-Mel@SiO_2 NPs. The inset image shows a color map of fluorescent intensity in ROI. (b, right) Target to background ratios (TBR) of the normal tissue and tumor after the injection of TRITC-labeled Gd-Mel@SiO_2 NPs. (c) Three-dimensional (3D) views that were reconstructed with coronal MR images of pre- (c, first) and postinfusion (c, second and third) of TRITC-labeled Gd-Mel@SiO_2 NPs. High MR T_1

contrast area was delineated as ROI which contains both injection trajectory and delivered region of TRITC-labeled Gd-Mel@ SiO_2 NPs, as indicated with red color. (c, fourth) A coregistered image combining a projection of 3D ROI from MR and two-dimensional (2D) fluorescent images of the detected TRITC-labeled Gd-Mel@SiO_2 NPs. (d) Temperature mapping images before and after radiation of NIR. Human prostate tumor xenograft mice were treated with multimodal image guided infusion of TRITC-labeled Gd-Mel@SiO_2 NPs. (inset) A digital image of focused NIR light on the region of infused. The scale of temperature is indicated in a color bar. (d, rightmost) Time-dependent temperature increase (ΔT) of tumor regions with and without TRITC-labeled Gd-Mel@SiO_2 NPs, when NIR was radiated with the power of 188 mW/cm^2. (e) Haematoxylin and Eosin (H&E), terminal deoxynucleotidyl transferase dUTP nick end labeling (TUNEL), and heat shock protein 70 (HSP 70) stained histological images of tumors without and with TRITC-labeled Gd-Mel@SiO_2 NPs, collected after NIR radiation with power of 188 mW/cm^2 for 3 min.